Insights into the Reaction Mechanisms of Nongraphitic High-Surface Porous Carbons for Application in Na- and Mg-Ion Batteries

Saúl Rubio, Rafaela Ruiz, Wenhua Zuo,* Yixiao Li, Ziteng Liang, Daniel Cosano, Jun Gao, Yong Yang,* and Gregorio F. Ortiz*

ABSTRACT: The fabrication of low-cost carbon materials and high-performance sodium- and magnesium-ion batteries comprising hierarchical porous electrodes and superior electrolytes is necessary for complementing Li-ion energy storage. In this work, nongraphitic high-surface porous carbons (NGHSPCs) exhibited an unprecedented formation of n-stages (stage-1 and stage-2) due to the co-intercalation of sodium $(Na(dgm)_2C_{20})$ with diglyme. X-ray diffraction patterns, Patterson diagram, Raman spectra, and IR spectra suggested the presence of n-stages. This phenomenon implies an increase of the initial capacity ($\sim$200 mAh g^{-1}) and good Na-ion diffusion (2.97×10^{-13} cm^2 s^{-1}), employing diglyme as compared to standard electrolytes containing propylene carbonate and fluoroethylene carbonate. Additionally, the current approach is scalable to full Na- and Mg-ion cells by using t-Na$_5$V(PO$_4$)$_2$F$_2$ and MgMnSiO$_4$ cathodes, respectively, reaching 250 and 110 W h kg^{-1} based on the anode mass. The simultaneous Mg (de)insertion from/into MgMnSiO$_4$ and the adsorption/desorption of bistriflimide ions on the NGHSPC surface is responsible for capacity enhancement.

KEYWORDS: porous carbon, high surface area, diglyme, sodium, co-intercalaction, bistriflimide, magnesium

1. INTRODUCTION

The major scientific challenge in developing sustainable sodium-ion batteries (SIBs) resides on the search of anode and cathode materials with sufficient capacity and cyclability.[1−3] Up until now, several anode materials display some inherent limitations such as large volume expansion/contraction, high overpotential related to the alloying electrodes, and scarce electronic conductivity related with organic compounds or with transition material-based oxides.[4−7] So far, on the progress made in the development of a SIB anode, carbon anode materials have been the dominant candidates preferred for their compatible reversible capacity with cathodes, low sodium storage voltage, and outstanding cycling stability.[8−10] On the other hand, the storage of magnesium ion properties in carbon materials also attracts the attention of the scientific community because it encountered intercalation behavior and enabled reversible charge transport via double-layer capacitance (EDLC).[11−13]

One of the main tasks of Mg-ion and Na-ion batteries is the selection of the appropriate electrolyte solution and electroactive materials. For instance, corrosive properties have a limited stability window causing electrolyte decomposition above 1.5 V vs Mg/Mg^{2+} when utilizing the Grignard reagents, and therefore the compatibility of the electrode materials must be considered.[14,15] Indeed, defective 2D graphene and graphene allotropes could be used as high-capacity anode materials for Mg-ion batteries.[16] Intercalated fullerides with
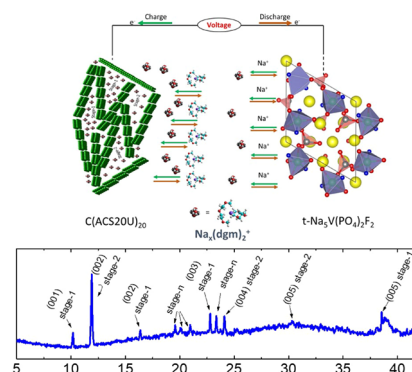
Mg$_2$C$_{60}$ stoichiometry were obtained by a solid-state reaction between C$_{60}$ and Mg.[11] The theoretical calculations support that solvated Mg ions with linear ether solvents (dimethoxyethane (DME)/diethylene glycol dimethyl ether (DGM)) promote a favorable co-intercalation mechanism with graphite, thus surpassing the limited capacity of Mg intercalation into natural graphite (35 mA h g^{-1}).[12,17] Nevertheless, little information is still reported in the literature about the intercalation of Mg ions in other kinds of carbon materials, and further research is required to understand the fundamental mechanism.[18]

In the past decade, glyme-based electrolytes were considered as great contenders to reversibly achieve sodium co-intercalation into graphitic materials. Among them, graphite,[19] graphitic petroleum cokes,[20] graphitic nanofibers,[21] and expanded graphites[22] should be highlighted because they demonstrated that the thermodynamic limitations of Na-ion storage can be abated. Indeed, Jensen et al.[23] highlighted a proper adaptability of sodium into graphite as sodium−glyme complexes, a reaction which is not possible for sodium in a
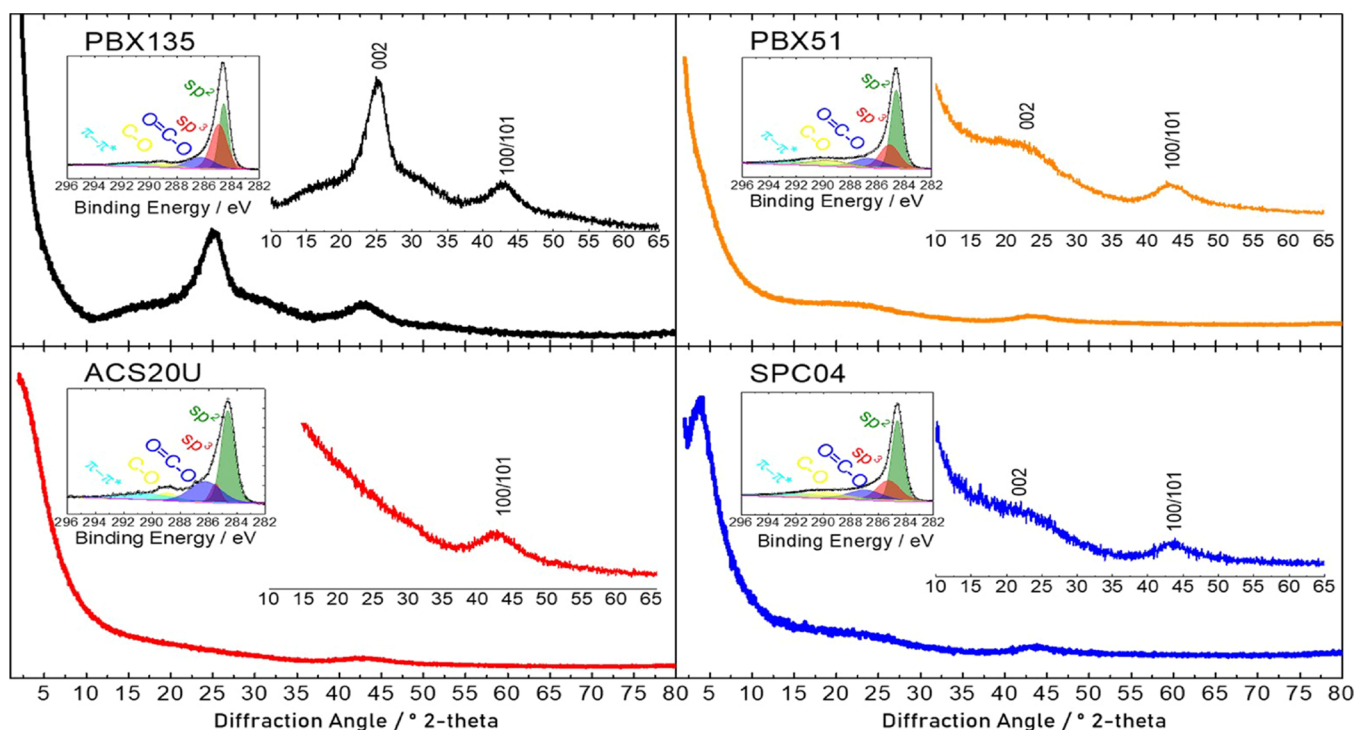
Figure 1. (A) X-ray diffraction patterns (XRD) of pristine NGHSPC (PBX135, PBX51, ACS20U, and SPC04) materials. Insets: X-ray photoelectron spectroscopy (XPS) showing the C 1s core level.

conventional electrolyte (1 M $NaClO_4$ in PC:FEC (98:2)). Also, the electrolyte adaptability is successfully transferred to layered-, nasicon- and transition-metal oxide-type compounds.[24−28]

The purpose of this work is the utilization of nongraphitic high-surface porous carbons (NGHSPCs), which are supplied by China Steel Chemical Corp., for application in both Na-ion and Mg-ion batteries. The main characteristic of these samples is the extremely high surface area, the values of which are 1880.9, 1702.5, and 1354.2 m^2 $g^{−1}$ for ACS20, SPC04, and PBX51, respectively. For comparison purpose, another active carbon (labeled as PBX135) with a lower surface area (131.2 m^2 $g^{−1}$) is used. Furthermore, the search of an adept electrolyte and cathode (t-$Na_5V(PO_4)_2F_2$ and $MgMnSiO_4$) to accomplish both Na-ion and Mg-ion batteries is explained in this work. For instance, for sodium-ion batteries, we utilized 1 M $NaClO_4$-PC:FEC (98:2) and 1 M $NaPF_6$-DGM electrolytes and found sodium co-intercalation and the consequent *n*-stages in a glyme-based electrolyte. A mixture of stage-1 and stage-2 has been detected by XRD, IR, and Raman spectra which differed according to the different morphological and functional groups. This can explain the increased capacity during the first 255 cycles for PBX135, 175 cycles for ACS20U, 75 cycles for PBX51, and 50 for SPC04. On the other hand, we have explored the advantages of the NGHSPC samples in Mg-ion cells and highlighted the importance of the surface area for achieving high-capacity batteries. Indeed, in the Mg-ion battery field, the use of activated carbon is attracting the attention of the scientific community because it enables reversible charge transport via EDLC due to its high surface area using 0.5 M $Mg(TFSI)_2$-AN (AN: acetonitrile) ($TFSI^−$, bistriflimide anion: $C_{11}H_{20}N_2F_6S_2O_4$) electrolyte.[11−13,29−32]

The novelty about the utilization of nongraphitic high-surface porous carbon materials is noticed for Na-ion cells in the mechanism of reaction showing an unprecedented formation of *n*-stages (stage-1 and stage-2), forming Nax-$(dgm)_2C_{20}$ complexes at the bulk state. The reported results of NGHSPCs open new opportunities to search alternative high-surface porous carbons that could react with sodium through the co-intercalation phenomenon, but special attention should be paid to avoid the structure degradation in either the bulk or the surface of the carbon-based materials to improve the cycling stability. Moreover, in Mg-ion cells, we proved the importance of using high-surface carbon materials to develop a hybrid battery/capacitor system based on the simultaneous Mg(*de*)insertion from/into the $MgMnSiO_4$ cathode and adsorption/desorption of $[TFSI]^−$ ions on the anode, as deduced by electrochemical, ICP, and EPR measurements.

2. EXPERIMENTAL SECTION

2.1. Materials and Electrochemistry. The samples used as the negative electrode are provided by China Steel Chemical Corp., and they are identified as ACS20U, SPC04, PBX51, and PBX135. In general, they are labeled as NGHSPC samples. The electrodes are prepared by mixing a 90:10 weight ratio mixture of NGHSPCs and polyvinylidene fluoride (PVdF) binder. Then, they are spread onto aluminum (for Na cells) and titanium foils (for Mg cells), followed by drying for 2 h at 120 °C under dynamic vacuum. An activation cycle of NGHSPCs in Na cells with a standard electrolyte ($NaClO_4$-PC) is performed before cycling the cells in a diglyme-based electrolyte. The area of the electrode is 0.64 cm^2. The areal mass loading fluctuates between 3.12 and 4.68 mg $cm^{−2}$ in the experiments performed with 2−3 mg of active material, respectively.

The sample used as a positive electrode material in Na-ion full cells is t-$Na_5V(PO_4)_2F_2$ which is prepared by a two-step reaction, as reported elsewhere.[33] We tested its suitability with 1 M $NaPF_6$-DGM electrolyte in sodium half-cells before the assembly of Na-ion full cells. On the other hand, the $MgMnSiO_4$ cathode used for Mg-ion cells is prepared by a sol−gel procedure and then heated at 900 °C, as reported earlier by our group.[34] The cathodes are prepared by mixing and spreading an 80:10:10 weight ratio mixture of active materials (t-$Na_5V(PO_4)_2F_2$ or $MgMnSiO_4$), carbon black, and polyvinylidene

fluoride (PVDF) binder onto aluminum or titanium foils and then drying for 2 h at 120 °C under dynamic vacuum. The capacity and energy density of the Na-ion full cell are determined based on the mass of the anode side.

Electrochemical impedance spectroscopy (EIS) is performed using an SP-150 BioLogic apparatus at an open-circuit voltage at the selected depth discharge and charge stages. The cells are relaxed for 1 h to reach the quasi-equilibrium state. The spectra are recorded by perturbing the open-circuit voltage with an AC signal of 10 mV from 100 kHz to 5 mHz.

The four NGHSPC anodes are subjected to a deep study of Na half-cells with two types of electrolytes: (i) 1 M NaPF$_6$-DGM and (ii) 1 M NaClO$_4$ in PC:FEC (98:2). The ACS20U anode was selected for combining the Na-ion full cell with t-Na$_5$V(PO$_4$)$_2$F$_2$. However, due to the high surface area of the four NGHSPC samples, all of them have been employed as anodes with MgMnSiO$_4$ in Mg-ion full cells and 0.5 M Mg(TFSI)$_2$-AN (AN: acetonitrile) electrolyte, and the potential has been measured versus Mg^{2+}/Mg. The capacity and energy density of the Mg-ion full cell are determined based on the mass of the anode side. The following reagents are supplied from commercial suppliers: DGM (Sigma Aldrich, 99% purity), NaPF$_6$ (Strem Chemicals, 99% purity), NaClO$_4$ (Sigma Aldrich, 98% purity), PC (Sigma Aldrich, 99.7% purity), FEC (Sigma Aldrich, 99% purity), Na foil (Panreac, 99.8% purity), Mg ribbons (Sigma-Aldrich, 99.5% purity), Mg-bistriflimide (Aldrich, 99.95%), and AN (Sigma Aldrich, 99.8%).

2.2. Material Characterization. The co-intercalation of Na$^+$-(diglyme)$_x$ is investigated by Raman spectroscopy using a Renishaw Raman instrument (InVia Raman microscope), with 532 nm laser radiation, equipped with a Leica microscope. Ex-situ IR data are obtained with a Bruker Tensor 27 FT-MIR spectrophotometer with CsI beam splitters and a DTGS detector. OPUS version 6.5 software is used to collect the transmission spectra. X-ray diffraction (XRD) patterns are recorded on a BrukerD8 Discover A25 diffractometer with Cu Kα radiation at a scan rate of 0.02° s^{-1} between 2 and 90° (2-θ°). TEM images are recorded on a JEOL 1400 microscope. SEM images are studied with a JEOL-SM6300 microscope equipped with an energy-dispersive X-ray spectrometer. The isotherms are used to calculate the specific surface area and total pore volume using the Brunauer−Emmett−Teller (BET) model. The pore size distributions and micropore volume are determined using the density functional theory (DFT) approach. An XPS instrument (SPECS Phoibos 150 MCD) using a monochromatic Al Kα source is used, and the internal standard is the C 1s line of adventitious carbon at 284.6 eV. EPR spectra are obtained on an EMX micro-X-band instrument at 295 K (Bruker) with a resonance frequency of 9.75 GHz. Inductively coupled plasma mass spectrometry (ICP-MS) is performed with a NexION 350X apparatus from PerkinElmer (Waltham, MA, USA). A microwave system UltraWave by Milestone (Shelton, USA) is used for the digestion of the samples using a mixture of nitric acid and hydrofluoric acid (Suprapur de Merck).

3. RESULTS AND DISCUSSION

3.1. Insights of *n*-Stage Formation in NGHSPCs. As a typical porous carbon, the *(002)* and *(100)/(101)* Bragg diffraction patterns of graphite are scarcely detected at 20.5− 23° and 43° for NGHSPCs samples with high surface area (1880.9, 1702.5, and 1354.2 m^2 g^{-1} for ACS20U, SPC04, and PBX51, respectively, Figures 1 and 2, Note S1 and Table 1).[35] A gradual shift of the *(002)* and *(100)/(101)* diffraction patterns toward the higher angles of ca. 25.3 and 43.2° was observed for the sample with the lowest surface area (131.2 m^2 g^{-1} for PBX135). The appearance of a much broadened and the disappearance of the *(100)/(101)* and *(002)* diffraction peaks of the ACS20U sample indicate the lowest graphitizable behavior. The average interlayer distances (d$_{002}$) are 3.536(2), 3.846(3), and 3.758(5) Å for PBX135, PBX51, and SPC04 samples, respectively, while the *(002)* peak for ACS20U is not
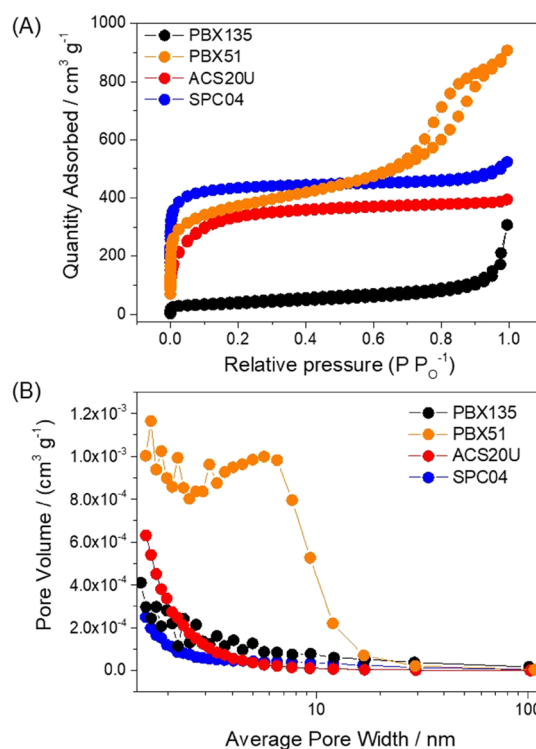
Figure 2. (A) Pore size distribution and (B) nitrogen adsorption− desorption isotherm curves of NGHSPCs.

observed, indicating that as the interlayer distance increased, a gradual decrease of the graphitization degree is observed.

A detailed information of the graphitization level of NGHSPC materials is gathered using Raman spectroscopy (Figure S1). The spectra of the pristine samples are characterized by two broadened bands at ca. 1350 and 1595 cm^{-1}, ascribed to the D1 and G modes belonging to sp^2 phases, respectively. The D1 mode is due to the lattice defects, disordered arrangement, and the low-symmetry carbon structure of graphite, while the G mode is assigned to an 'in-plane' displacement of ordered carbons in the hexagonal sheets.[36] The obtained graphitization index (I_D/I_G) for the pristine PBX135, PBX51, ACS20U, and SPC04 samples is 1, 0.92, 0.97, and 0.92, respectively. The NGHSPCs displayed a slight variation of the graphitization index after sodium co-intercalation; thus, the graphitization index changed to 1.08, 1, 0.94, and 0.84, respectively. Some changes of the G peak (the C−C stretching mode) have been associated to the formation of n-stage compounds during the Na$^+$−ether co-intercalation reaction in graphite and hence to the graphitization index.[28,37]

The Na test battery is a rich tool used to grasp changes in the chemical composition of materials such as in NGHSPCs, regardless of the typical electrochemical cycling behavior of different electrodes (Figure 3). Therefore, an unprecedented formation of *n*-stages in NGHSPC anodes is detected when utilizing the diglyme-based electrolyte in Na cells (Figures 4,BA, S2A−D, and S3). To grasp the reaction mechanism and the structural changes induced by the electrochemical sodium reaction, ex-situ XRD patterns are compared to that using 1 M NaClO$_4$ in PC:FEC (98:2) electrolyte (Figures 1 and S4). A harsh change for the four samples is observed after a complete discharge in 1 M NaPF$_6$-DGM electrolyte as compared with the original ones. Therefore, the significant band shifting of the few-layered graphenic order of the *(002)* reflection is a direct

Table 1. Surface Area, Pore Volume, Conductivity, Interlayer Distance, Ash, and Iron Contents of Pristine NGHSPC Samples

sample ID	BET surface area/m^2 g^{-1}	conductivity/S mm^{-1}	total pore volume/cm^3 g^{-1}	ash content/%	iron content/ppm	average interlayer distance/Å
PBX135	131.2	0.602	0.48		<20	3.536(2)
PBX51	1354.2	0.313	1.4		<40	3.846(3)
ACS20U	1880.9	0.346	0.88	0.06		
SPC04	1702.5	0.180	0.81	0.35	16	3.758(5)
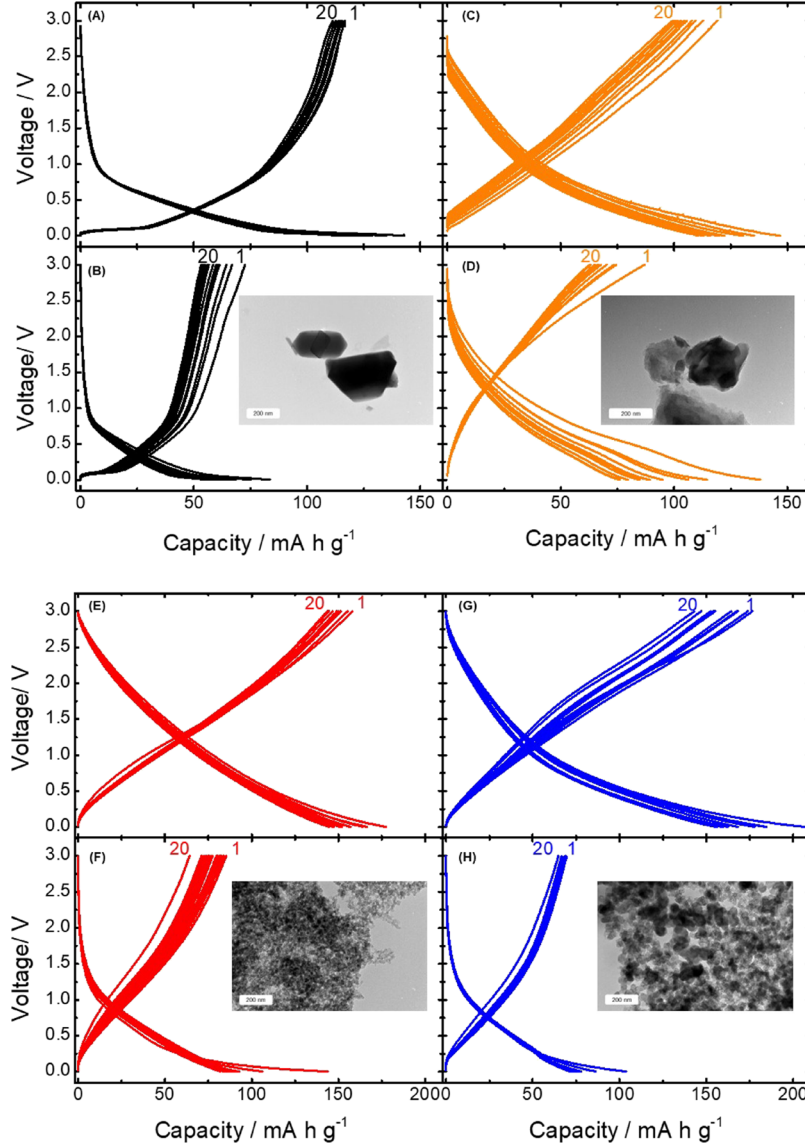
Figure 3. Galvanostatic discharge/charge curves of the first 20 cycles comparing the electrochemical characteristics of NGHSPC anodes in Na half-cells for: (A, C, E, G) PBX135, PBX51, ACS20U, and SPC04 in 1 M NaPF$_6$-DGM and (B, D, F, and H) PBX135, PBX51, ACS20U, and SPC04 in 1 M NaClO$_4$-PC:FEC (98:2) electrolytes, respectively. The insets represent the TEM measurements showing monodispersed morphology of NGHSPCs.

proof of sodium co-intercalation. As is observed, the formation of n-stages (stage 1 and stage-2) takes place at the end of the discharge (Table S1, Figures 4A$_1$, B$_1$, and S2A−D).

The methodology used to calculate the stage number can be found in previous literature that explained the Na-ion storage in graphite using solvated Na-ion intercalation and forming ternary GICs.[19,38] Nevertheless, the formation of solvated Na-ion intercalation in nongraphitic high-surface porous carbon remained unexplored, so far. The (002) peak at 20−25° (2θ) of the NGHSPCs splits into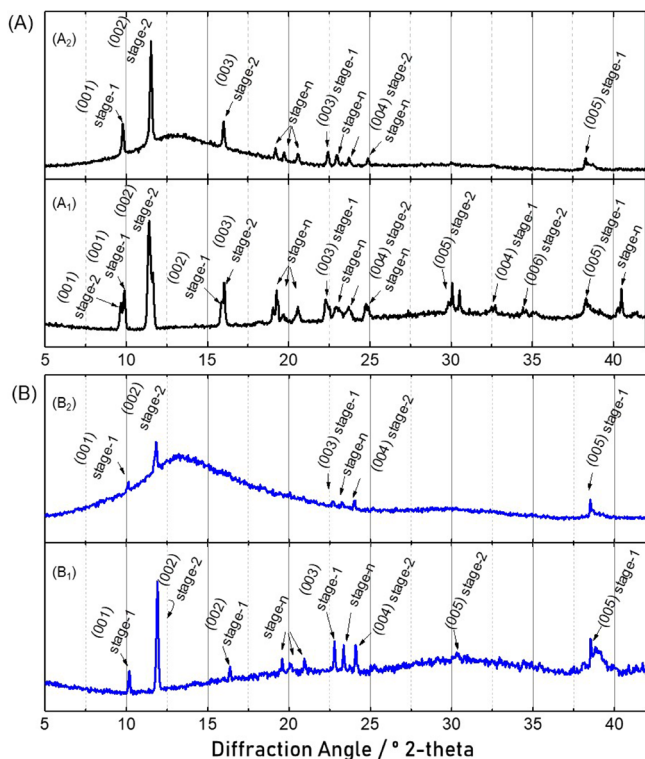 several peaks that are indexed as (00l) and (00l + 1).[38−40] Applying Bragg's law, the l-value can be determined using the following equations:[41]

$$d_{(00l)} = \frac{I_c}{l} \text{ and } d_{(00l+1)} = \frac{I_c}{l+1} \tag{1}$$

$$d_{(00l)}\sin\theta_{(00l)} = d_{(00l+1)}\sin\theta_{(00l+1)} \tag{2}$$

$$l = \frac{1}{\left[\frac{\sin\theta_{00l+1}}{\sin\theta_{00l}} - 1\right]} \tag{3}$$

Figure 4. Ex situ XRD patterns of (A) PBX135 and (B) SPC04 recorded after (B₂,C₂) full discharge and (B₁,C₁) subsequent charge in Na half-cells using 1 M NaPF₆-DGM electrolyte.

where I_c is the c lattice parameter of each stage of GIC matching the repeated distance, and $d_{(00l)}$ and $d_{(00l+1)}$ are, respectively, the d-spacing values of the $(00l)$ and $(00l + 1)$ planes. The consecutive changes during discharge can be followed during partial discharge at 1, 0.4, and 0.2 V for the NGHSPC anodes (Figure S2). The measurements of θ_{00l} and θ_{00l+1} at this stage suggest that the peaks (001) at 9.63°, (005) at 30°, and (006) at 34.4° of stage-2, peaks (002) at 15.8° and (004) at 32.6° of stage-1, and the peak at 40.5° (2-theta) of stage-n disappeared, and the rest of the peaks decreased in intensity after charging (Figure 4A₁,A₂). Likewise, from the measurements of θ_{00l} and θ_{00l+1} of the SPC04 sample, it is observed that the (002) peak at 16.34° of stage-1, (005) peak at 30.3° of stage-2, and the peaks at 19.6, 20 and 21° (2-theta)

of stage-n disappeared, and the rest of the peaks located at 30.3° and 41.8° (2-theta) decreased in intensity after charging, and the intensity of the peaks at 10.2, 11.9, 22.7, 23.3, 24.1, and 38.6° (2-theta) decreased (Figure 4B₁,B₂). The most important difference is that these n-stages are not detected for fully discharged electrodes in 1 M NaClO₄ in the PC:FEC (98:2) electrolyte (Figure S4). These carbonate-based solvents only permit unsolvated sodium intercalation forming the binary intercalation compounds.[42] On charging up to 3.0 V, the XRD patterns are not completely recovered to the original state, but a partial restoration of the n-stages is inferred. The desolvation of Na⁺ is not complete as it is normally found in the graphite-based anodes.[19,20,28] This fact can be deduced from the XRD results through the appearance and disappearance of a group of diffraction patterns observed between the discharge and charge processes. The schematic representation of the formation of $Na_x(dgm)_2C_{20}$ in a NGHSPC anode reflects the differences found with the typical Na⁺ adsorption in NGHSPCs using carbonate-based electrolytes (Figure 5).

3.2. Pseudocapacitive Behavior of NGHSPC Compared with Low-Surface-Area Graphite and Hard Carbon. Dou et al.[43] and Doeff et al.[44] reported data of hard carbons and activated carbons, indicating that sodium and diglyme hardly co-intercalate to form ternary intercalation compounds. However, Dong et al.[45] utilized hard carbons of 292 and 563 m² g⁻¹ and found a slight carbon layer expansion in which the (002) diffraction peak shifted 1.52° (2-theta) corresponding to an enlargement of 0.301 Å of d-spacing and suggested the formation of ternary intercalation complexes (Na⁺−DEGDME−carbon). Our work targets the study of NGHSPC anodes with 6.4-fold and 3.3-fold higher surface area (Note S1, Table 1, and Figure 2) and showed a clear formation of $Na_x(dgm)_2C_{20}$, indicative of a much higher enlargement of d-spacing of the (002) diffraction peak of ca. 5.39 and 5.59 Å for SPC04 and PBX135, respectively (Tables 1 and S1). Monodispersed morphology with homogeneous particle sizes of 20, 35, 250, and 400 nm is observed for ACS20U, SPC04, PBX51, and PBX135, respectively (insets of Figure 3). Therefore, a nanometric character of the particles is evident from the TEM measurements.

Materials possessing a high degree of graphitization and low surface area are rather known to exhibiting such properties.[19−23] As far as we know, it is the first time the n-stages are encountered in NGHSPCs. For the sake of comparison, the PBX135 anode suffers a splitting of the (002) diffraction peak
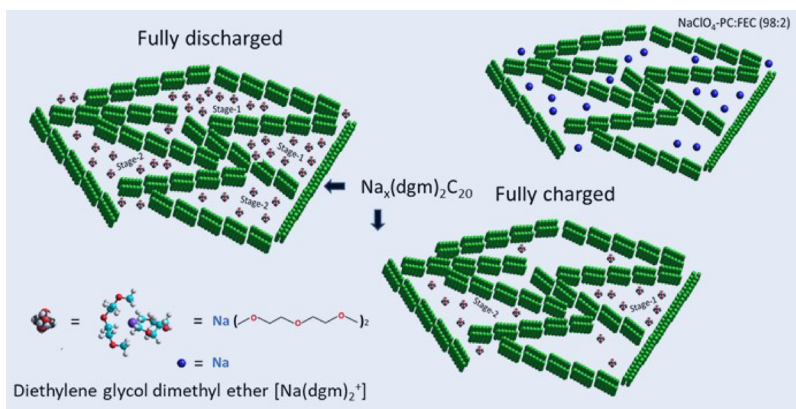
Figure 5. Schematic representation of Na(dgm)₂⁺ co-intercalation found in NGHSPCs with the formation of $Na_x(dgm)_2C_{20}$ and its comparison with the typical Na⁺ adsorption in defects/edges using carbonate-based electrolytes.

at 9.67° (9.13 Å), 15.85° (5.58 Å), 22.27° (3.98 Å), 32.73° (2.73 Å), 38.30° (2.34 Å), 48.85° (1.87 Å), and 55.63° (1.65 Å), which correspond to the (001), (002), (003), (004), (005), (006), and (007) reflections of stage-1 similar to graphite.[46] These lines coexist with some lines formed from previous n-stages (ca. stage-2 and n-stages, with n > 2) that usually occurred for moderately discharged electrodes which are observed at 11.5, 19.15, 19.76, 20.63, 23.03, 23.75, 25, 32.73, 34.6, and 40.4° (2-theta), implying a high shift in the interlayer expansion (Table S1). For SPC04, PBX51, and ACS20U anodes, similar changes are observed with similar intensity of n-stage peaks. The selected DGM solvent is a flexible linear ether-based compound with high polarity, which is able to co-intercalate with sodium ions to form ternary intercalation compounds with NGHSPCs.[46]

Different facets of the electrochemical behavior of NGHSPCs in Na cells with 1 M $NaPF_6$-DGM and 1 M $NaClO_4$-PC:FEC(98:2) electrolytes are observed in terms of capacity and cyclability (Figures 3 and 6). The galvanostatic
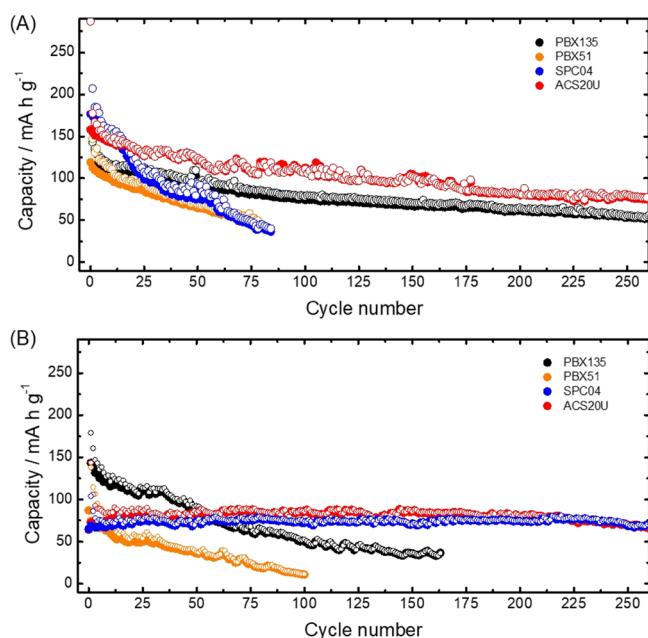
Figure 6. Electrochemical cycling performance of NGHSPC anodes achieved up to 250 cycles for both (A) 1 M $NaPF_6$-DGM and (B) 1 M $NaClO_4$ in PC:FEC (98:2) electrolytes. Note: the cells were cycled at C/2 rate.

discharge/charge curves for the 1 M $NaPF_6$-DGM electrolyte can be divided into two voltage parts: (i) 3−1 V the voltage decay swiftly providing 8, 40, 75, and 40 mA h g^{-1} and (ii) 1.0−0.003 V less attenuated voltage drop, providing 136, 107,

103, and 148 mA h g^{-1} capacity for PBX135, PBX51, ACS20U, and SPC04 (Figure 3,C,E,GA). The last three samples exhibit a sloping potential curve in the whole voltage range, and the former sample resembles sodium insertion into the micropores of a pseudographitic order at a low-potential voltage plateau.[42] The galvanostatic profiles follow a similar trend in the 1 M $NaClO_4$- PC:FEC(98:2) electrolyte but with almost twofold decreased capacity for PBX135, ACS20U, and SPC04 and 1.5-fold for PBX51 (Figure 2B,D,F,H). During the sodium co-intercalation reaction and the formation of n-stages (stage-1, stage-2, etc.) in graphite, graphitic petroleum coke or thermally expanded graphite is typically observed with a voltage plateau near to 1, 0.8, and 0.6 and a constant voltage decay at 0.6−0.001 V versus Na^+/Na,[19,20,22,41] while the formation of n-stages in these NGHSPC materials occurred with a different galvanostatic profile in which a sloping potential curve from 3 to 0.001 V is observed. Then, the main difference in the galvanostatic curves of NGHSPCs (with extremely high surface area, Figure 2, Table 1, and Note S1) versus the known electrochemical profile of hard carbons and graphite (with low surface area)[43−45] is the absence of the potential stage during the galvanostatic discharge. The reported results of NGHSPCs open new opportunities to search alternative high-surface porous carbons that could react with sodium through the co-intercalation phenomenon, but special attention to avoid the structure degradation in either the bulk or surface of the carbon-based materials should be paid to improve the cycling stability.[28,41]

For the sake of clarity, the data of the first discharge capacity (FDC in mA h g^{-1}) obtained from the preactivation cycle in Na cells and 1 M $NaClO_4$-PC:FEC (98:2) electrolyte are provided in Table 2. It should be clarified that prior to assembling the Na half-cells with NGHSPC anodes in 1 M $NaPF_6$-DGM electrolyte, a preactivation cycle in Na half-cell in $NaClO_4$-PC:FEC(98:2) electrolyte is carried out (Figure S5). The second discharge capacities are labeled as SDC-DGM and SDC-PC (in mA h g^{-1}) which are obtained using 1 M $NaPF_6$-DGM- and 1 M $NaClO_4$-PC(2% FEC)-based electrolytes, respectively.

The initial reversible capacities are 147, 142.7, 172.1, and 207 in 1 M $NaPF_6$-DGM-based and 138, 178.9, 158.2, and 104 mA h g^{-1} in 1 M $NaClO_4$-PC:FEC(98:2)-based electrolytes for PBX135, PBX51, ACS20U, and SPC04, respectively (Figure 3). The most outstanding properties are observed for ACS20U with DGM-based electrolytes with 172.1 mA h g^{-1} of reversible capacity and 60% of capacity retention over 250 cycles. The SPC04 anode in a PC-based electrolyte has a capacity of 104 mA h g^{-1} which can be retained around 67% over 250 cycles. Also, ACS20U in the 1 M $NaClO_4$-PC:FEC (98:2) electrolyte exhibited good capacity retention with an initial capacity of 158.2 and 45% of retention over 250 cycles.

Table 2. Data of the First Discharge Capacity (FDC in mA h g^{-1}) Obtained from the Preactivation Cycle in Na Cells and 1 M $NaClO_4$-PC:FEC(98:2) Electrolyte[a]

sample ID	FDC (mAh g^{-1})	SDC-DGM (mAh g^{-1})	SDC-PC (mAh g^{-1})	E_f-DGM (%)	E_f-PC (%)
PBX51	305.4	142.7	138	46.7	45.1
PBX135	345.2	147	178.9	42.6	51.8
ACS20U	503.1	172.1	158.2	34.2	31.4
SPC04	399.2	207	104	51.8	26.1

[a]The second discharge capacities are labeled as SDC-DGM and SDC-PC (in mA h g^{-1}), which are obtained using 1 M $NaPF_6$-DGM- and 1 M $NaClO_4$-PC(2% FEC)-based electrolytes, respectively. The efficiency is deduced from the SDC/FDC ratio.

This fact is correlated by the apparent diffusion coefficients (2.29×10^{-14} cm^2 s^{-1}/2.97×10^{-13} cm^2 s^{-1}) and the interfacial charge transfer (0.2 ohm g) and surface layer (0.12 ohm g) resistances obtained in ether-based electrolytes (Figures 7, S7, Table S2, and Note S2). A slight fluctuation
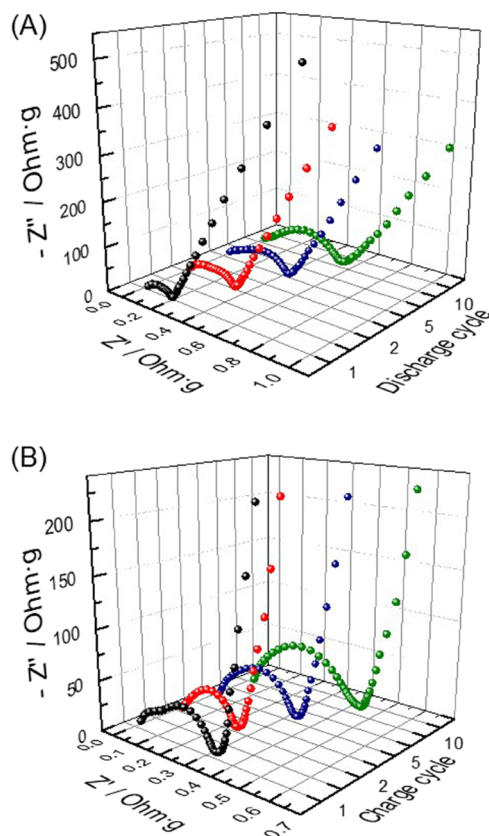
Figure 7. (A,B) Nyquist plots of the selected ACS20U sample, recorded on discharge and charge from 1st−10th cycles using 1 M NaPF$_6$-DGM electrolyte.

in their values at the end of the charge and discharge is exhibited, suggesting a thin solid electrolyte interface film on the surface. Most of this improvement can be ascribed to the accomplishments of electrode materials capable to provide a fast and stable diffusion path to the sodium−glyme complexes. Specifically, the use of diglyme-based electrolytes improved the capacity during the first 255 cycles for PBX135, 175 cycles for ACS20U, 75 cycles for PBX51, and 50 for SPC04 (Figure S6), showing that the structural degradation in some of the samples occurred earlier than that in others.
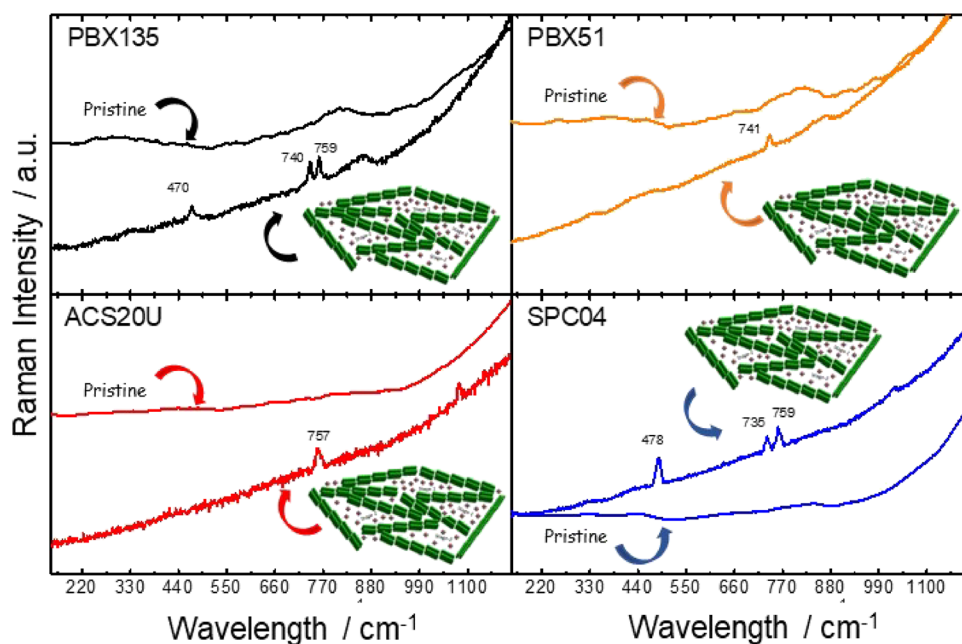
The energetics of the intercalated products primarily determine the difference in the overall Na storage voltage.[41] Moreover, as reported by Kim et al.,[41] from in operando synchrotron X-ray diffraction, it is observed that graphite suffers a phase-like transformation with many different stages changing sensitively with a small alteration in the sodium content. Specifically, during the discharge at 31 mA h g^{-1} (Na/C: 1/72, 1.5 h of reaction), stage n GIC is formed, at 46−80 mA h g^{-1} (Na/C: 1/50, 15−2.2 h) another o GIC phase is formed at the expense of stage n GIC, and after the biphasic reaction into the stage o GIC, the stage p GIC emerges from 50 until ~110 mA h g^{-1} (Na/C: 1/28−1/21, ~4−6 h). These n, o, and p GIC stages presented the c lattice parameters of 18.5, 15.06, and 11.62 Å whose differences between I_c values are

nearly 3.44 Å.[41] In graphite exists a reversible structural transformation implying stable capacity. However, the observed result for our NGHSPC materials indicated that there is no complete recovery of the XRD peaks after charging, and this could be indicative of a structural degradation, because of which we observed different cyclability (Figures S6 and 6).
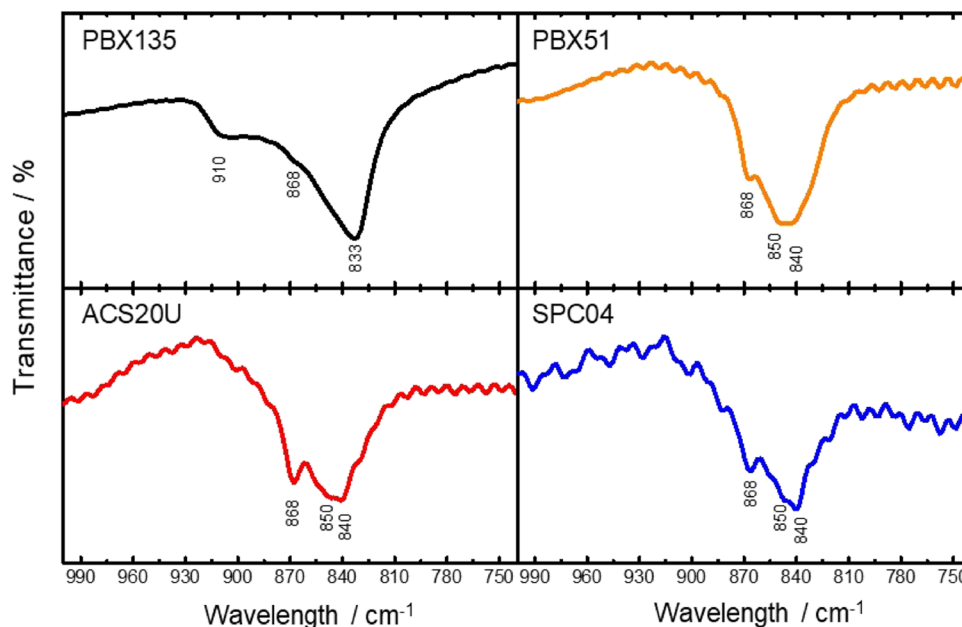
3.3. Raman, IR, and Patterson Data after Na Co-Intercalation into NGHSPCs. Raman spectra confirmed the changes from pristine and discharged electrodes (Figure 8). A set of new peaks at 470, 740, and 759 cm^{-1} appeared in different proportions for each sample, indicating that diglyme solvates Na$^+$ ions to form the Na$_x$(dgm)$_2$C$_{20}$ complex (Figure 5).[47] The peaks are reported to be a particular band of solvating glyme with s-block metal cations.[48] These peaks are compared to that of diglyme solvating Mg^{2+} ions, and the Raman shift position differed very slightly due to a different charge/radius ratio and concomitant weaker cation−solvent interactions of Na$^+$ (95 pm) and Mg^{2+} (65 pm). Moreover, the coordination can be discussed from diglyme's band because the diglyme solvent shows a peak at 860−865 cm^{-1} which is ascribed to the free diglyme. These Na$_x$(dgm)$_2$C$_{20}$ complexes are characteristic of the different nature of NGHSPCs. Hence, Na(dgm)$_2$$^+$ can access through the defects into few graphenic sheets, several substituent groups which serve as reactive sites to potentially increase the sodium co-intercalation, the open surface porosity, and micorpore walls, as observed through SEM and XPS (insets of Figures 1, S8, and S9, Notes S3 and S4, and Table S3).[49] In addition, the IR spectra of the fully discharged electrodes revealed a broad band at ~880 cm^{-1} (Figure 9). This mode is attributed to two diglyme molecules coordinated by a sodium ion, with the dihedral angle sequence of each diglyme molecule of O−C−C−O (conformation about the O−C bond and C−O bond is trans, and the conformation about the C−C bond is gauche) and O−C−C−O (idem as before, but with gauche minus), attributed to Na$_x$(dgm)$_2$C$_{20}$ stage-1 in graphitic petroleum coke.[20] Additionally, ethylene oxide units with gauche OCCO torsional angles have bands in the range from 825 to 890 cm^{-1}.[50] The arrangement of sodium co-intercalated between NGHSPCs is modeled by the 1D Patterson diagram, which is created from the *(00l)* diffraction peak intensities (Figure 10). The peak maxima for Na−C, C−C, C−O, and O−O distances are 5.85, 2.85, 5.52, and 8.42 Å in the c-axis of the unit cell, respectively, as similarly observed for commercial graphite.[20,22] These bonds correspond to the two diglyme molecules necessary to reach a stable shell in dilute solution. These features certainly support the existence of n-stages.

3.4. Full Na- and Mg-Ion Cells. Full Na-ion cells with diglyme-based electrolytes are evaluated. First, it is worth noting that trigonal sodium vanadium fluorophosphate (t-Na$_5$V(PO$_4$)$_2$F$_2$) is selected as a cathode because it exhibits a high operation voltage and long cycling life (ca. 1000 cycles), as recently reported by Liang et al.[33] However, a preliminary examination of a fresh 1 M NaPF$_6$-DGM electrolyte in a Na half-cell is done between 4.1 and 2.5 V (Figure 11A). The galvanostatic charge−discharge cycle exhibits one sodium (de)-insertion involving the V^{4+}/V^{3+} redox pair. The main cathodic peaks at around 3.42 and 3.52 V and anodic peaks at 3.52 and 3.35 V imply a small voltage polarization entailing good reversibility during 250 cycles due to its stable framework (Figure S10). To further verify the proposed scientific strategy, the full Na-ion C(ACS20U)$_{20}$/1 M NaPF$_6$-DGM/t-Na$_5$V-(PO$_4$)$_2$F$_2$ cell is assembled and cycled under C/2 rate (Figure
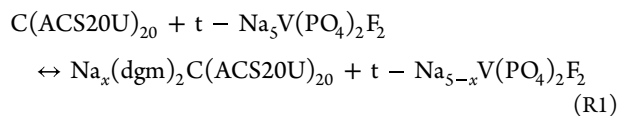
Figure 8. Raman spectra recorded in the spectral range of 150−1200 cm^{-1} for pristine NGHSPC samples and after discharge in sodium cells using 1 M NaPF$_6$-DGM electrolyte.
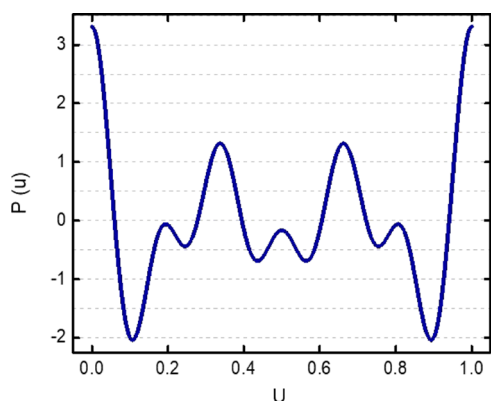

Figure 9. Detailed view of the IR spectra at the fully discharged state of NGHSPC anodes (PBX135, PBX51, ACS20U, and SPC04) obtained from sodium cells using 1 M NaPF$_6$-DGM electrolyte.

11B). The overall reaction of the full cell can be summarized as follows:

$$C(ACS20U)_{20} + t - Na_5V(PO_4)_2F_2$$

$$\leftrightarrow Na_x(dgm)_2C(ACS20U)_{20} + t - Na_{5-x}V(PO_4)_2F_2 \tag{R1}$$

The experimental capacity delivered by t-Na$_5$V(PO$_4$)$_2$F$_2$ is 66 mA h g^{-1} (for $x = 1.0$) and that of C(ACS20U)$_{20}$ is 172.1 mA h g^{-1} ($x = 1.0$). The mass of the cathode is adapted to fully obtain the galvanostatic profile of the full cell based on the anode side $(m+/m- > 2.6)$. As estimated from their individual voltages, the combination of C(ACS20U)$_{20}$ with t-Na$_5$V-

(PO$_4$)$_2$F$_2$ gives rise to a battery operating in the 4.0−0.7 V range. The galvanostatic profile during charge implied the sodium transfer from t-Na$_5$V(PO$_4$)$_2$F$_2$ to the carbon anode (C(ACS20U)$_6$), and through the discharge, sodium transferred back from Na$_x$(dgm)$_2$C(ACS20U)$_{20}$ to t-Na$_{5-x}$V(PO$_4$)$_2$F$_2$ (Figures 11B and 12A). Then, the reversible capacity of the Na-ion full cell is 141 and 126.2 mA h g^{-1}, as measured on the charge and discharge states, respectively. Cycle efficiency of >90% and average potential reaction of ∼2.0 V are observed, entailing an energy density of 250 W h kg^{-1} cycled a C/2 rate based on the mass of the anode side (retained 85 mA h g^{-1} over 110 cycles, Figure 4D). This result compares well with other Na-ion full HC-21-1400/1 M NaPF$_6$-EC:DMC/O3-
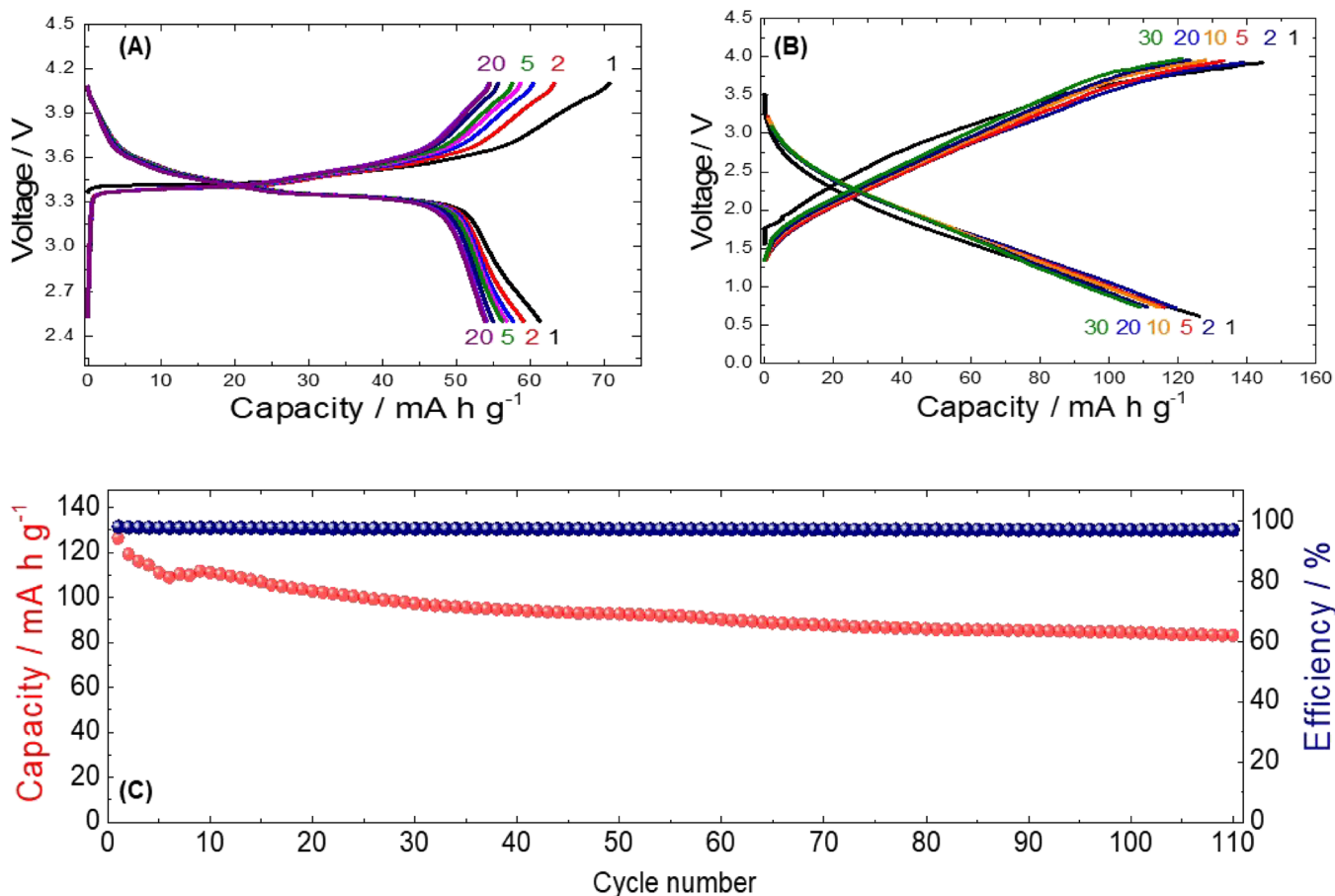
Figure 10. Patterson analysis of electron density after sodium insertion along the *c*-axis (SPC04 sample).

$NaNi_{1/3}Fe_{1/3}Mn_{1/3}O_2$,[51] graphite/1 M $NaPF_6$-DGM/ $Na_3V_2(PO_4)_3$,[52] or $VO_2/1$ M $NaClO_4$-EC-PC/ $Na_3(VO)_2(PO_4)_2F$,[53] cells with ca. 300, 131, and 215 W h kg^{-1} energy density, respectively.

Because an extremely high surface area of carbon anodes is desired for reversible charge transport via the EDLC for Mg-ion batteries,[11−13,29−32] several experiments about the suitability of NGHSPC anodes are shown below. It is worth mentioning that according to Gershinsky et al.,[30] ion adsorption/desorption processes in the electric double layer (EDL) are usually fully reversible. They prepared counter

electrodes, based on high surface area, the active carbon cloth electrodes, whose total surface area is high enough to allow a full charge balance for the Mg intercalation process with V_2O_5. Moreover, Cabello et al.[54] combined a h-MoO_3 cathode and an active carbon anode forming a hybrid or an asymmetrical electrochemical capacitor where the mechanism of reaction in the working electrode is more complex than Mg^{2+}-(de)-insertion. Anion $[TFSI]^-$ adsorption and redox of oxygen ions in the lattice of h-MoO_3 can contribute to the reversible capacity, defining the working electrode (h-MoO_3) as a dual-ion electrode material.

Four Mg-ion full cells are assembled with different NGHSPC anodes, 0.5 M $Mg(TFSI)_2$-AN electrolyte, and $MgMnSiO_4$ cathode. Based on the simultaneous Mg (de)-insertion from/into $MgMnSiO_4$ and the adsorption/desorption of $[TFSI]^-$ ions on the anode, the system is considered as a hybrid battery/capacitor (Figure 12B).[30,54,55] From the galvanostatic profiles are deduced high-polarization faradic and non-faradic processes that contributed to the total capacity. The experimental charge/discharge capacities are 36/30, 173/193, 469/368, and 245/204 mA h g^{-1} for cells that utilized PBX135, PBX51, ACS20U, and SPC04 anodes, respectively (Figures 13A and S11). Theoretically, 156 mA h g^{-1} is assigned to 0.5 de-inserted Mg^{2+} from $MgMnSiO_4$ (reaction #2).[34] The ICP results confirmed the extraction of 0.46 Mg^{2+} corresponding to 143.5 mA h g^{-1}, which is related to the reachable specific charge (Table 3). By combining the results of the electrochemical curves with the ICP measure-

Figure 11. Galvanostatic charge/discharge profiles of: (A) t-$Na_5V(PO_4)_2F_2$ vs metallic sodium in 1 M $NaPF_6$-DGM electrolyte at C/2 rate, (B) Na-ion (ACS20U/1 M $NaPF_6$-DGM/t-$Na_5V(PO_4)_2F_2$) cell cycled at C/2 rate, and (C) cycling performance of the full Na-ion cell specified in (B).
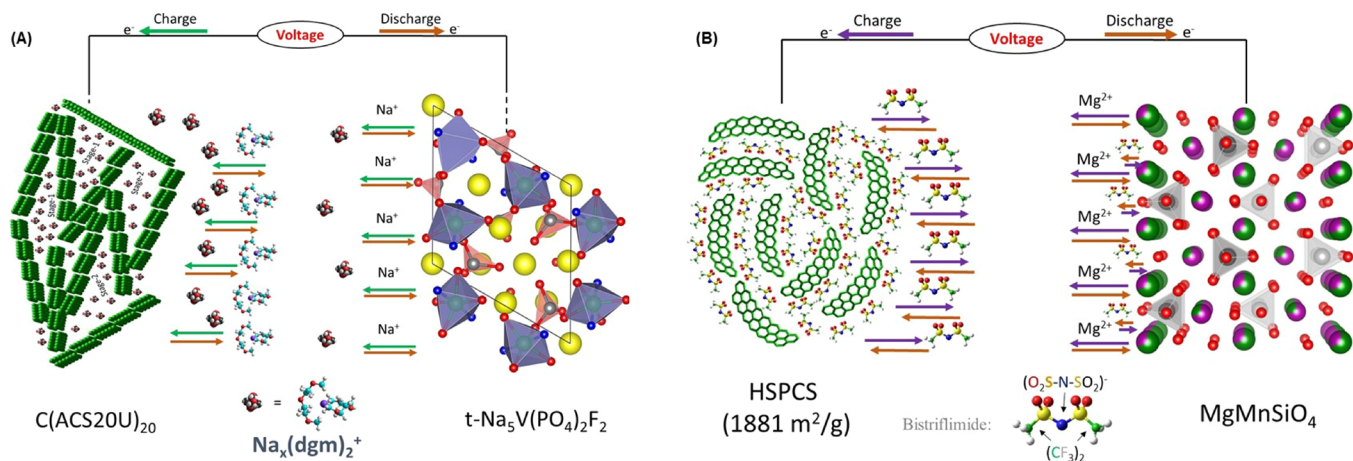
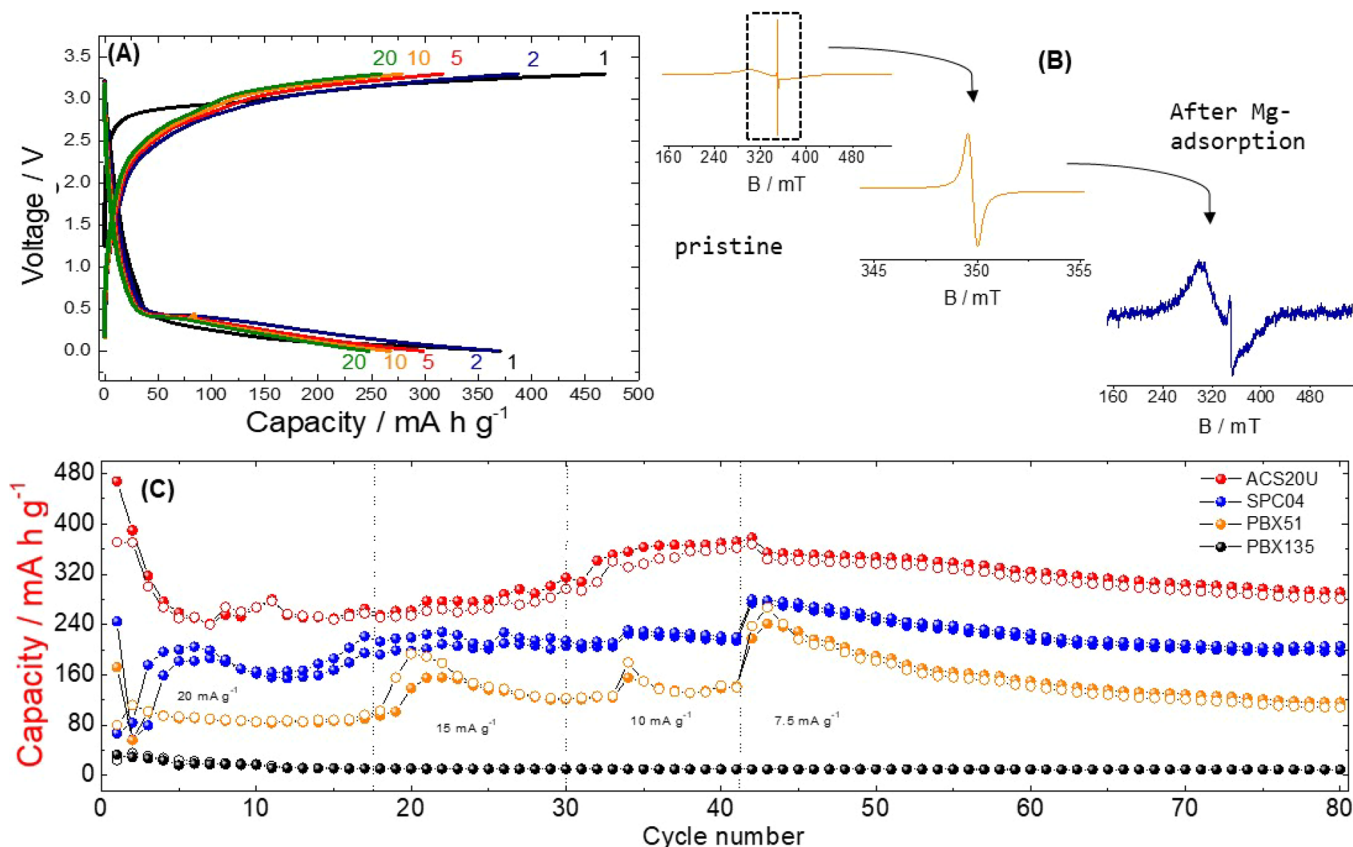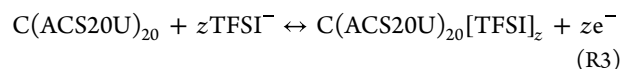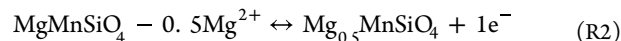**Figure 12.** Schematic representation of (A) Na-ion and (B) Mg-ion cells.

Figure 13. (A) Galvanostatic charge/discharge curves of the Mg-ion ACS20U/0.5 M Mg(TFSI)$_2$-AN/MgMnSiO$_4$ cell. (B) EPR response of pristine ACS20U (orange line) and discharged ACS20U electrode (blue line). (C) Cycling performance of several Mg-ion full cells: ACS20U/0.5 M Mg(TFSI)$_2$-AN/MgMnSiO$_4$ (red color symbols), SPC04/0.5 M Mg(TFSI)$_2$-AN/MgMnSiO$_4$ (blue color symbols), PBX51/0.5 M Mg(TFSI)$_2$-AN/MgMnSiO$_4$ (orange color symbols), and PBX135/0.5 M Mg(TFSI)$_2$-AN/MgMnSiO$_4$ (black color symbols).

Table 3. ICP Results Showing the Mg:Mn Atomic Ratio of Pristine MgMnSiO$_4$ and after Reaction in the ACS20U/0.5 M Mg(TFSI)$_2$-DME/MgMnSiO$_4$ Cell

MgMnSiO$_4$ sample	Mg:Mn ratio (theoretical)	Mg:Mn ratio (ICP)
pristine	1:1	1.03:1
charged	0.5:1	0.57:1
charged/discharged	1:1	1.01:1

ments, it is observed that the extra capacity could be attributed to the adsorption of bistriflimide ([TFSI]$^-$) ions and/or

magnesium ions on the surface of the carbons.[55] From the ICP results, a negligible amount of magnesium is measured in the ACS20U anode (<0.001%) after the first charge of the full cell. Therefore, the observed extra capacity is attributed to the adsorption of [TFSI]$^-$ ions on the carbon surface.[30] Then, the following reactions can be deduced:

$$MgMnSiO_4 - 0.5Mg^{2+} \leftrightarrow Mg_{0.5}MnSiO_4 + 1e^- \quad (R2)$$

$$C(ACS20U)_{20} + zTFSI^- \leftrightarrow C(ACS20U)_{20}[TFSI]_z + ze^- \quad (R3)$$

Therefore, the extra reversible capacity (measured on the charge state) is assigned to the adsorption of $[TFSI]^-$ ions on the high surface area of ACS20U (1881 m^2 g^{-1}), accounting for 325.5 ($z = 2.08$) mA h g^{-1}. On decreasing the surface area of the anodes, we observed the tendency of SPC04 (1703 m^2 g^{-1}) with 101.5 mA h g^{-1} (0.65e^-) and PBX51 (1454 m^2 g^{-1}) with 29.5 mA h g^{-1} (0.19e^-). Also, the lowest capacity (30 mA h g^{-1}) is obtained for the PBX135 (131 m^2 g^{-1}) anode which confirms the very low adsorption/desorption properties of $[TFSI]^-$ ions. Thus, the observed phenomena entail that a higher surface area can promote easier adsorption/desorption and higher capacity in Mg-ion cells. The adsorption properties of weak host−guest molecules are determined by EPR, where the molecules confined in porous systems may show the activity of bulk material as well as nanoscale particles. The pristine ACS20U sample is chosen to examine the influence of guest molecules on the electronic properties of NGHSPCs. The EPR spectrum changes significantly after the adsorption of bistriflimide molecules. A case example with the strongest effect is observed in the case of water adsorption.[56] The signal due to delocalized electrons undergoes significant changes compared to the signal coming from free radicals (Figure 13B).

Certainly, the galvanostatic profiles are different from previous literature reports. Truong et al.[57] investigated the electrochemical performance of $MgMnSiO_4$ versus activated carbon (Maxsorb MSC-30) anode and 0.5 M $Mg(ClO_4)_2$-acetonitrile electrolyte by galvanostatic cycles between −1.0 and 1.0 V versus C or 3.2 and 1.6 V versus Mg^{2+}/Mg at C/50. This narrow voltage window limited the capacity to 90 mA h g^{-1} and did not provide a proof of the reversible charge transport via EDLC. In that work, details of the surface area of activated carbon were not provided, and wider voltage windows to explore the possible adsorption of $[ClO_4]^-$ were not provided either. However, several studies used high surface area-activated carbons and wider voltages, enabling a reversible charge transport via EDLC.[11−13,29−32] In addition, our recent work[34] described the performance of several Mg-ion full cells where one of them used activated carbon (Fluka, S_{BET} = 1200 m^2 g^{-1}) as the anode, $C@MgMnSiO_4$ as the cathode, and 0.5 M $Mg(TFSI)_2$ in DME (dimethoxyethane) electrolyte. The full cells combined an insertion cathode and a EDLC anode.[34] The observed charge capacity is high (314 mA h g^{-1}), ascribed to the simultaneous Mg (de)-insertion at the cathode and $[TFSI]^-$adsorption on the anode surface.

At 50% of the state of charge (SOC) and 50% of the state of discharge (SOD), the capacities are 15, 96, 184, and 102 mA h g^{-1} and 2.03, 2.74, 2.72, and 2.75 V for the full cells employing PBX135, PBX51, ACS20U, and SPC04 anodes, respectively. Considering an average potential of 0.6 V, the energy density is 9, 58, 110, and 61 W h kg^{-1}, respectively. Over 80 cycles, this capacity/energy density can be retained by about 33, 97, 76, and 96%, respectively (Figure 13C). The rate performance is explored using rates of 20, 15, 10, and 7.5 mA g^{-1}. Comparing with the literature, the experimentally observed capacity of V_2O_5 at around 2.3 V versus Mg^{2+}/Mg implied a high energy density of 660 W h kg^{-1}.[58] Referring to the voltage equivalency between the activated carbon (AC) and Mg^{2+}/Mg redox couple is quite important. For example, a different equivalency of voltages is found in the literature: (i) 0 V of AC = 1.5 V of Mg^{2+}/Mg,[59] (ii) 0 V of AC = 2.2 V of Mg^{2+}/Mg,[58] and (iii) 0 V of AC = 2.45 V Mg^{2+}/Mg.[60] Hence, a difference of voltage of ∼1 V in the calculated equivalency from AC to Mg^{2+}/Mg for

an electrode material with 100 mA h g^{-1} capacity could lead to a significant fluctuation in the estimation of the energy density.

4. CONCLUSIONS

The NGHSPC samples provided by China Steel Chemical Corporation have been shown to exhibit novel properties, as observed from the electrochemical and chemical characterizations. The NGHSPC samples with a negligible graphitic order exhibited an unprecedented formation of *n*-stages due to sodium co-intercalation with diglyme, and a clear expansion of the interlayer distance of the carbon slabs is detected. By an adept selection of the electrolyte (ca. diglyme and bistriflimide) and cathode with robust structure (ca. t-Na_5V-$(PO_4)_2F_2$ and $MgMnSiO_4$), the Na- and Mg-ion full cells could provide a stable capacity and energy density of 250 and 110 W h kg^{-1}, respectively. Attending to their extremely high surface area, nanometric particle size, X-ray amorphousness, interpenetrated pore volume, low graphitic/hydrocarbon proportion, high conductivity, and proper chemical composition, these results are rather promising. The XRD patterns, Patterson diagram, Raman, and IR spectra undoubtedly detected a mixture of stage-1 and stage-2 in the first cycle, which suggests the formation of $Na_x(dgm)_2C_{20}$ complexes occurring in the bulk state. Seldom literature reported *n*-stage formation into high-surface-area carbons (or activated carbons), except for materials with graphitic order (e.g., graphite). The reported results of NGHSPCs open new opportunities to search alternative high-surface porous carbons that could react with sodium through the co-intercalation phenomenon, but special attention to avoid the structure degradation in either the bulk or the surface of the carbon-based materials should be paid to improve the cycling stability. We observed that the intercalation of solvated Na^+ into graphite domains will break down the structure of these domains, and that is why a continuous decay of the capacity on cycling is observed. Further studies to understand the correlation between the *n*-stages and successful reversible capacity associated with the complete appearance and disappearance of stages will be the subject of future studies.

■ ASSOCIATED CONTENT

● Supporting Information

The Supporting Information is available free of charge at https://pubs.acs.org/doi/10.1021/acsami.2c09237.

> Experimental part and Notes 1−4; additional figures including XRD patterns, diffusion coefficients calculation, SEM images and XPS analyses; electrochemical cycling life of t-$Na_5V(PO4)_2F_2$ in diglyme; electrochemical discharge−charge curves of Mg-ion full cells employing PBX135, PBX51, ACS20U and SPC04 anodes versus $MgMnSiO_4$ cathode; and Tables 123 with data of Interlayer *d*-spacing of NGHSPCs samples after sodium co-intercalation, Warburg impedance, diffusion coefficients and XPS (PDF)

■ AUTHOR INFORMATION

Corresponding Authors

Wenhua Zuo − Helmholtz Institute Ulm (HIU), Karlsruhe Institute of Technology (KIT), Ulm 89081, Germany; ⦿ orcid.org/0000-0003-1977-2775; Email: wenhua.zuo@kit.edu

Yong Yang − *State Key Laboratory for Physical Chemistry of Solid Surfaces, Department of Chemistry, College of Chemistry and Chemical Engineering, Xiamen University, Xiamen 361005, China;* ⓘ orcid.org/0000-0002-9928-7165; Email: yyang@xmu.edu.cn

Gregorio F. Ortiz − *Department of Inorganic Chemistry and Chemical Engineering, University Research Institute in Nanochemistry (IUNAN), University of Córdoba, Córdoba E-14071, Spain;* ⓘ orcid.org/0000-0003-3104-8018; Email: q72maorg@uco.es

Authors

Saúl Rubio − *Department of Inorganic Chemistry and Chemical Engineering, University Research Institute in Nanochemistry (IUNAN), University of Córdoba, Córdoba E-14071, Spain*

Rafaela Ruiz − *Department of Inorganic Chemistry and Chemical Engineering, University Research Institute in Nanochemistry (IUNAN), University of Córdoba, Córdoba E-14071, Spain*

Yixiao Li − *State Key Laboratory for Physical Chemistry of Solid Surfaces, Department of Chemistry, College of Chemistry and Chemical Engineering, Xiamen University, Xiamen 361005, China*

Ziteng Liang − *State Key Laboratory for Physical Chemistry of Solid Surfaces, Department of Chemistry, College of Chemistry and Chemical Engineering, Xiamen University, Xiamen 361005, China*

Daniel Cosano − *Department of Organic Chemistry, University Research Institute in Nanochemistry (IUNAN), University of Córdoba, Córdoba E-14071, Spain*

Jun Gao − *State Key Laboratory for Physical Chemistry of Solid Surfaces, Department of Chemistry, College of Chemistry and Chemical Engineering, Xiamen University, Xiamen 361005, China*

Complete contact information is available at:
https://pubs.acs.org/10.1021/acsami.2c09237

Notes

The authors declare no competing financial interest.

■ REFERENCES

(1) Zuo, W.; Qiu, J.; Liu, X.; Ren, F.; Liu, H.; He, H.; Luo, C.; Li, J.; Ortiz, G. F.; Duan, H.; Liu, J.; Wang, M. S.; Li, Y.; Fu, R.; Yang, Y. The Stability of P2-layered Sodium Transition Metal Oxides in Ambient Atmospheres. *Nat. Commun.* **2020**, *11*, 3544.

(2) Liu, X.; Zhong, G.; Xiao, Z.; Zheng, B.; Zuo, W.; Zhou, K.; Liu, H.; Liang, Z.; Xiang, Y.; Chen, Z.; Ortiz, G. F.; Fu, R.; Yang, Y. Al and Fe-containing Mn-based Layered Cathode with Controlled Vacancies for High-Rate Sodium Ion Batteries. *Nano Energy* **2020**, *76*, No. 104997.

(3) Qi, Y.; Tong, Z.; Zhao, J.; Ma, L.; Wu, T.; Liu, H.; Yang, C.; Lu, J.; Hu, Y.-S. Scalable Room-Temperature Synthesis of Multi-Shelled $Na_3(VOPO_4)_2F$ Microsphere Cathodes. *Joule* **2018**, *2*, 2348−2363.

(4) Liu, Z.; Yu, X.-Y.; Lou, X.-W. (. D.).; Paik, U. Sb@C Coaxial Nanotubes as a Superior Long-Life and High-Rate Anode for Sodium Ion Batteries. *Energy Environ. Sci.* **2016**, *9*, 2314−2318.

(5) Ortiz, G. F.; Hanzu, I.; Lavela, P.; Knauth, P.; Tirado, J. L.; Djenizian, T. Nanoarchitectured TiO_2/SnO: A Future Negative Electrode for High Power Density Li-Ion Microbatteries? *Chem. Mater.* **2010**, *22*, 1926−1932.

(6) Park, Y.; Shin, D.-S.; Woo, S. H.; Choi, N. S.; Shin, K. H.; Oh, S. M.; Lee, K. T.; Hong, S. Y. Sodium Terephthalate as an Organic Anode Material for Sodium Ion Batteries. *Adv. Mater.* **2012**, *24*, 3562−3567.

(7) Fu, S.; Ni, J.; Xu, Y.; Zhang, Q.; Li, L. Hydrogenation Driven Conductive $Na_2Ti_3O_7$ Nanoarrays as Robust Binder-Free Anodes for Sodium-Ion Batteries. *Nano Lett.* **2016**, *16*, 4544−4551.

(8) Hou, H.; Qiu, X.; Wei, W.; Zhang, Y.; Ji, X. Carbon Anode Materials for Advanced Sodium-Ion Batteries. *Adv. Energy Mater.* **2017**, *7*, No. 1602898.

(9) Darwiche, A.; Marino, C.; Sougrati, M. T.; Fraisse, B.; Stievano, L.; Laure Monconduit, L. Better Cycling Performances of Bulk Sb in Na-Ion Batteries Compared to Li-Ion Systems: An Unexpected Electrochemical Mechanism. *J. Am. Chem. Soc.* **2012**, *134*, 20805−20811.

(10) Dou, X.; Hasa, I.; Saurel, D.; Vaalma, C.; Wu, L.; Buchholz, D.; Bresser, D.; Komaba, S.; Passerini, S. Hard Carbons for Sodium-Ion Batteries: Structure, Analysis, Sustainability, and Electrochemistry. *Mater. Today* **2019**, *23*, 87−104.

(11) Pontiroli, D.; Aramini, M.; Gaboardi, M.; Mazzani, M.; Gorreri, A.; Riccò, M.; Margiolaki, I.; Sheptyakov, D. Ionic conductivity in the Mg Intercalated Fullerene Polymer Mg_2C_{60}. *Carbon* **2013**, *51*, 143−147.

(12) God, C.; Bitschnau, B.; Kapper, K.; Lenard, C.; Schmuck, M.; Mautner, F.; Koller, S. Intercalation Behaviour of Magnesium into Natural Graphite Using Organic Electrolyte Systems. *RSC Adv.* **2017**, *7*, 14168−14175.

(13) Yoo, H. D.; Shterenberg, I.; Gofer, Y.; Gershinsky, G.; Pour, N.; Aurbach, D. Mg Rechargeable Batteries: An On-Going Challenge. *Energy Environ. Sci.* **2013**, *6*, 2265−2279.

(14) Muldoon, J.; Bucur, C. B.; Oliver, A. G.; Sugimoto, T.; Matsui, M.; Kim, H. S.; Allred, G. D.; Zajicek, J.; Kotani, Y. Electrolyte Roadblocks to a Magnesium Rechargeable Battery. *Energy Environ. Sci.* **2012**, *5*, 5941−5950.

(15) Imhof, R.; Haas, O.; Novák, P. Magnesium Insertion Electrodes for Rechargeable Nonaqueous Batteries, a Competitive Alternative to Lithium? *Electrochim. Acta* **1999**, *45*, 351−367.

(16) Er, D.; Detsi, E.; Kumar, H.; Shenoy, V. B. Defective Graphene and Graphene Allotropes as High-Capacity Anode Materials for Mg Ion Batteries. *ACS Energy Lett.* **2016**, *1*, 638−645.

(17) Kim, D. M.; Jung, S. C.; Ha, S.; Kim, Y.; Park, Y.; Ryu, J. H.; Han, Y. K.; Lee, K. T. Cointercalation of Mg^{2+} Ions into Graphite for Magnesium-Ion Batteries. *Chem. Mater.* **2018**, *30*, 3199−3203.

(18) Imamura, D.; Miyayama, M. Characterization of Magnesium-Intercalated V_2O_5/Carbon composites. *Solid State Ionics* **2003**, *161*, 173−180.

(19) Jache, B.; Adelhelm, P. Use of Graphite as a Highly Reversible Electrode with Superior Cycle Life for Sodium-Ion Batteries by Making Use of Co-Intercalation Phenomena. *Angew. Chem., Int. Ed.* **2014**, *53*, 10169−10173.

(20) Cabello, M.; Chyrka, T.; Klee, R.; Aragón, M. J.; Bai, X.; Lavela, P.; Vasylchenko, G. M.; Alcántara, R.; Tirado, J. L.; Ortiz, G. F.

Treasure Na-Ion Anode from Trash Coke by Adept Electrolyte Selection. *J. Power Sources* **2017**, *347*, 127−135.

(21) Nacimiento, F.; Cabello, M.; Ortiz, G. F.; Alcántara, R.; Lavela, P.; Tirado, J. L. Morphological Adaptability of Graphitic Carbon Nanofibers to Enhance Sodium Insertion in a Diglyme-Based Electrolyte. *Dalton Trans.* **2019**, *48*, 5417−5424.

(22) Cabello, M.; Bai, X.; Chyrka, T.; Ortiz, G. F.; Lavela, P.; Alcántara, R.; Tirado, J. L. On the Reliability of Sodium Co-Intercalation in Expanded Graphite Prepared by Different Methods as Anodes for Sodium-Ion Batteries. *J. Electrochem. Soc.* **2017**, *164*, A3804−A3813.

(23) Jensen, A. C. S.; Au, H.; Gärtner, S.; Titirici, M. M.; Drew, A. J. Solvation of $NaPF_6$ in Diglyme Solution for Battery Electrolytes. *Batter. Supercaps* **2020**, *3*, 1306−1310.

(24) Zuo, W.; Liu, R.; Ortiz, G. F.; Rubio, S.; Chyrka, T.; Lavela, P.; Zheng, S.; Tirado, J. L.; Wang, D.; Yang, Y. Sodium Storage Behavior of $Na_{0.66}Ni_{0.33-x}Zn_xMn_{0.67}O_2$ (x = 0, 0.07 and 0.14) Positive Materials in Diglyme-Based Electrolytes. *J. Power Sources* **2018**, *400*, 317−324.

(25) Westman, K.; Dugas, R.; Jankowski, P.; Wieczorek, W.; Gachot, G.; Morcrette, M.; Irisarri, E.; Ponrouch, A.; Palacín, M. R.; Tarascon, J.-M.; Johansson, P. Diglyme Based Electrolytes for Sodium-Ion Batteries. *ACS Appl. Energy Mater.* **2018**, *1*, 2671−2680.

(26) Rubio, S.; Maça, R. R.; Aragón, M. J.; Cabello, M.; Castillo-Rodríguez, M.; Lavela, P.; Tirado, J. L.; Etacheri, V.; Ortiz, G. F. Superior Electrochemical Performance of TiO_2 Sodium-Ion Battery Anodes in Diglyme-Based Electrolyte Solution. *J. Power Sources* **2019**, *432*, 82−91.

(27) Xiao, B.; Soto, F. A.; Gu, M.; Han, K. S.; Song, J.; Wang, H.; Engelhard, M. H.; Murugesan, V.; Mueller, K. T.; Reed, D.; Sprenkle, V. L.; Balbuena, P. B.; Li, X. Lithium-Pretreated Hard Carbon as High-Performance Sodium-Ion Battery Anodes. *Adv. Energy Mater.* **2018**, *8*, No. 1801441.

(28) Li, Y.; Wu, F.; Li, Y.; Liu, M.; Feng, X.; Bai, Y.; Wu, C. Ether-Based Electrolytes for Sodium Ion Batteries. *Chem. Soc. Rev.* **2022**, *51*, 4484−4536.

(29) Ruch, P. W.; Cericola, D.; Hahn, M.; Kotz, R.; Wokaun, A. On the Use of Activated Carbon as a Quasi-Reference Electrode in Non-Aqueous Electrolyte Solutions. *J. Electroanal. Chem.* **2009**, *636*, 128−131.

(30) Gershinsky, G.; Yoo, H. D.; Gofer, Y.; Aurbach, D. Electrochemical and Spectroscopic Analysis of Mg^{2+} Intercalation into Thin Film Electrodes of Layered Oxides: V_2O_5 and MoO_3. *Langmuir* **2013**, *29*, 10964−10972.

(31) Feng, Z.; Chen, X.; Qiao, L.; Lipson, A. L.; Fister, T. T.; Zeng, L.; Kim, C.; Yi, T.; Sa, N.; Proffit, D. L.; Burrell, A. K.; Cabana, J.; Ingram, B. J.; Biegalski, M. D.; Bedzyk, M. J.; Fenter, P. Phase-Controlled Electrochemical Activity of Epitaxial Mg-Spinel Thin Films. *ACS Appl. Mater. Interfaces* **2015**, *7*, 28438−28443.

(32) Kaveevivitchai, W.; Jacobson, A. J. High Capacity Rechargeable Magnesium-Ion Batteries Based on a Microporous Molybdenum−Vanadium Oxide Cathode. *Chem. Mater.* **2016**, *28*, 4593−4601.

(33) Liang, Z.; Zhang, X.; Liu, R.; Ortiz, G. F.; Zhong, G.; Xiang, Y.; Chen, S.; Mi, J.; Wu, S.; Yang, Y. New Dimorphs of $Na_5V(PO_4)_2F_2$ as an Ultrastable Cathode Material for Sodium-Ion Batteries. *ACS Appl. Energy Mater.* **2020**, *3*, 1181−1189.

(34) Rubio, S.; Liang, Z.; Li, Y.; Zuo, W.; Lavela, P.; Tirado, J. L.; Liu, R.; Zhou, K.; Zhu, J.; Zheng, B.; Liu, X.; Yang, Y.; Ortiz, G. F. Exploring Hybrid Mg^{2+}/H^+ Reactions of $C@MgMnSiO_4$ with Boosted Voltage in Magnesium-Ion Batteries. *Electrochim. Acta* **2022**, *404*, No. 139738.

(35) Kamiyama, A.; Kubota, K.; Nakano, T.; Fujimura, S.; Shiraishi, S.; Tsukada, H.; Komaba, S. High-Capacity Hard Carbon Synthesized from Macroporous Phenolic Resin for Sodium-Ion and Potassium-Ion Battery. *ACS Appl. Energy Mater.* **2020**, *3*, 135−140.

(36) Pan, D. Y.; Wang, S.; Zhao, B.; Wu, M. H.; Zhang, H. J.; Wang, Y.; Jiao, Z. Li Storage Properties of Disordered Graphene Nanosheets. *Chem. Mater.* **2009**, *21*, 3136−3142.

(37) Cohn, A. P.; Share, K.; Carter, R.; Oakes, L.; Pint, C. L. Ultrafast Solvent-Assisted Sodium Ion Intercalation into Highly Crystalline Few-Layered Graphene. *Nano Lett.* **2016**, *16*, 543−548.

(38) Kim, H.; Hong, J.; Park, Y.-U.; Kim, J.; Hwang, I.; Kang, K. Sodium Storage Behavior in Natural Graphite using Ether-based Electrolyte Systems. *Adv. Funct. Mater.* **2015**, *25*, 534−541.

(39) Seela, J. A.; Dahn, J. R. Electrochemical Intercalation of PF_6 into Graphite. *J. Electrochem. Soc.* **2000**, *147*, 892−898.

(40) Park, J.; Xu, Z. L.; Yoon, G.; Park, S. K.; Wang, J.; Hyun, H.; Park, H.; Lim, J.; Ko, Y. -J.; Yun, Y. S.; Kang, K. Stable and High-Power Calcium-Ion Batteries Enabled by Calcium Intercalation into Graphite. *Adv. Mater.* **2020**, *32*, No. 1904411.

(41) Kim, H.; Hong, J.; Yoon, G.; Kim, H.; Park, K. Y.; Park, M. S.; Yoon, W. S.; Kang, K. Sodium Intercalation Chemistry in Graphite. *Energy Environ. Sci.* **2015**, *8*, 2963−2969.

(42) Thomas, P.; Ghanbaja, J.; Billaud, D. Electrochemical Insertion of Sodium in Pitch-Based Carbon Fibres in Comparison with Graphite in $NaClO_4$−Ethylene Carbonate Electrolyte. *Electrochim. Acta* **1999**, *45*, 423−430.

(43) Dou, X.; Hasa, I.; Saurel, D.; Jauregui, M.; Buchholz, D.; Rojo, T.; Passerini, S. Impact of the Acid Treatment on Lignocellulosic Biomass Hard Carbon for Sodium-Ion Battery Anodes. *ChemSusChem* **2018**, *11*, 3276−3285.

(44) Doeff, M. M.; Ma, Y.; Visco, S. J.; De Jonghe, L. C. Electrochemical Insertion of Sodium into Carbon. *J. Electrochem. Soc.* **1993**, *140*, L169−L170.

(45) Dong, R.; Zheng, L.; Bai, Y.; Ni, Q.; Li, Y.; Wu, F.; Ren, H.; Wu, C. Elucidating the Mechanism of Fast Na Storage Kinetics in Ether Electrolytes for Hard Carbon Anodes. *Adv. Mater.* **2021**, *33*, No. 2008810.

(46) Zhu, Z.; Cheng, F.; Hu, Z.; Niu, Z.; Chen, J. Highly Stable and Ultrafast Electrode Reaction of Graphite for Sodium Ion Batteries. *J. Power Sources* **2015**, *293*, 626−634.

(47) Sagane, F.; Ogi, K.; Konno, A.; Kanamura, K. The Effect of Cyclic Ethers on Mg Plating/Stripping Reaction in Ionic Liquid Electrolytes. *J. Electrochem. Soc.* **2019**, *166*, A5054−A5058.

(48) Brouillette, D.; Irich, D. E.; Taylor, N. J.; Perron, G.; Odziemkowski, M.; Desnoyers, J. E. Stable Solvates in Solution of Lithium Bis(Trifluoromethylsulfone)Imide in Glymes and Other Aprotic Solvents: Phase Diagrams, Crystallography and Raman Spectroscopy. *Phys. Chem. Chem. Phys.* **2002**, *4*, 6063−6071.

(49) Li, Z.; Bommier, C.; Chong, Z. S.; Jian, Z.; Surta, T. W.; Wang, X.; Xing, Z.; Neuefeind, J. C.; Stickle, W. F.; Dolgos, M.; Greaney, P. A.; Ji, X. Mechanism of Na-Ion Storage in Hard Carbon Anodes Revealed by Heteroatom Doping. *Adv. Energy Mater.* **2017**, *7*, No. 1602894.

(50) Matsuura, H.; Fukuhara, K. Vibrational Spectroscopic Studies of Conformation of Poly(oxyethylene). II. Conformation Espectrum Correlations. *J. Polym. Sci. B Polym. Phys.* **1986**, *24*, 1383−1400.

(51) Meng, Q.; Lu, Y.; Ding, F.; Zhang, Q.; Chen, L.; Hu, Y. S. Tuning the Closed Pore Structure of Hard Carbons with the Highest Na Storage Capacity. *ACS Energy Lett.* **2019**, *4*, 2608−2612.

(52) Han, P.; Han, X.; Yao, J.; Liu, Z.; Cao, X.; Cui, G. Flexible Graphite Film with Laser Drilling Pores as Novel Integrated Anode Free of Metal Current Collector for Sodium ion Battery. *Electrochem. Commun.* **2015**, *61*, 84−88.

(53) Chao, D.; Lai, C.-H. (. M.).; Liang, P.; Wei, Q.; Wang, Y.-S.; Zhu, C. (. R.).; Deng, G.; Doan-Nguyen, V. V. T.; Lin, J.; Mai, L.; Fan, H. J.; Dunn, B.; Shen, Z. X. Sodium Vanadium Fluorophosphates (NVOPF) Array Cathode Designed for High-Rate Full Sodium Ion Storage Device. *Adv. Energy Mater.* **2018**, *8*, No. 1800058.

(54) Cabello, M.; Medina, A.; Alcantara, R.; Nacimiento, F.; Pérez-Vicente, C.; Tirado, J. L. A theoretical and Experimental Study of Hexagonal Molybdenum Trioxide as Dual-Ion Electrode for Rechargeable Magnesium Battery. *J. Alloys Compd.* **2020**, *831*, No. 154795.

(55) Cao, X.; Wang, L.; Chen, J.; Zheng, J. Low-Cost Aqueous Magnesium-Ion Battery Capacitor with Commercial Mn_3O_4 and Activated Carbon. *ChemElectroChem* **2018**, *5*, 2789−2794.

(56) Sato, H.; Kawatsu, N.; Enoki, T.; Endo, M.; Kobori, R.; Maruyama, S.; Kaneko, K. Physisorption-Induced Change in the Magnetism of Microporous Carbon. *Solid State Commun.* **2003**, *125*, 641−645.

(57) Truong, Q. C.; Devaraju, M. K.; Honma, I. Nanocrystalline $MgMnSiO_4$ and $MgCoSiO_4$ Particles for Rechargeable Mg-Ion Batteries. *J. Power Sources* **2017**, *361*, 195−202.

(58) Yoo, H. D.; Jokisaari, J. R.; Yu, Y. S.; Kwon, B. J.; Hu, L.; Kim, S.; Han, S. D.; Lopez, M.; Lapidus, S. H.; Nolis, G. M.; Ingram, B. J.; Bolotin, I.; Ahmed, S.; Klie, R. F.; Vaughey, J. T.; Fister, T. T.; Cabana, J. Intercalation of Magnesium into a Layered Vanadium Oxide with High Capacity. *ACS Energy Lett.* **2019**, *4*, 1528−1534.

(59) Rubio, S.; Liu, R.; Liu, X.; Lavela, P.; Tirado, J. L.; Li, Q.; Liang, Z.; Ortiz, G. F.; Yang, Y. Exploring the High-Voltage Mg^{2+}/Na^+ Co-Intercalation Reaction of $Na_3VCr(PO_4)_3$ in Mg-Ion Batteries. *J. Mater. Chem. A* **2019**, *7*, 18081−18091.

(60) Zeng, J.; Yang, Y.; Lai, S.; Huang, J.; Zhang, Y.; Wang, J.; Zhao, J. A Promising High-Voltage Cathode Material Based on Mesoporous $Na_3V_2(PO_4)_3$/C for Rechargeable Magnesium Batteries. *Chem. — Eur. J.* **2017**, *23*, 16898−16905.